The following resources related to this article are available online at
www.sciencemag.org (this infomation is current as of August 18, 2011):

Updated information and services, including high-resolution figures, can be found in the online version of this article at:
http://www.sciencemag.org/content/333/6045/993.full.html

Supporting Online Material can be found at:
http://www.sciencemag.org/content/suppl/2011/08/17/333.6045.993.DC1.html

This article **cites 21 articles**, 1 of which can be accessed free:
http://www.sciencemag.org/content/333/6045/993.full.html#ref-list-1

This article appears in the following **subject collections:**
Astronomy
http://www.sciencemag.org/cgi/collection/astronomy

and occasional extreme drought, coincident with fires in the tropics, represent the greatest risks to the continued large C sink in the world's forests (21, 24, 30, 37). A better understanding of the role of forests in biosphere C fluxes and mechanisms responsible for forest C changes is critical for projecting future atmospheric CO_2 growth and guiding the design and implementation of mitigation policies.

Reference and Notes

1. G. J. Nabuurs et al., in Climate Change 2007: Mitigation, B. Metz, O. R. Davidson, P. R. Bosch, R. Dave, L. A. Meyer, Eds. (Cambridge Univ. Press, Cambridge, 2007), pp. 542–584.
2. J. G. Canadell et al., Proc. Natl. Acad. Sci. U.S.A. 104, 18866 (2007).
3. S. Khatiwala, F. Primeau, T. Hall, Nature 462, 346 (2009).
4. C. Le Quéré et al., Nat. Geosci. 2, 831 (2009).
5. R. K. Dixon et al., Science 263, 185 (1994).
6. Details of data sources, accounting, and estimation methods used for each country, region, and C component are provided in the supporting online material.
7. Food and Agriculture Organization, Global Forest Resources Assessment 2010 (Food and Agriculture Organization, Rome, 2010), forestry paper 163.
8. A. Z. Shvidenko, D. G. Schepaschenko, S. Nilsson, in Basic Problems of Transition to Sustainable Forest Management in Russia, V. A. Sokolov, A. Z. Shvidenko, O. P. Vtorina, Eds. (Russian Academy of Sciences, Krasnoyarsk, Russia, 2007), pp. 5–35.
9. P. E. Kauppi et al., For. Ecol. Manage. 259, 1239 (2010).
10. W. A. Kurz, G. Stinson, G. J. Rampley, C. C. Dymond, E. T. Neilson, Proc. Natl. Acad. Sci. U.S.A. 105, 1551 (2008).
11. G. Stinson et al., Glob. Change Biol. 17, 2227 (2011).
12. R. Birdsey, K. Pregitzer, A. Lucier, J. Environ. Qual. 35, 1461 (2006).
13. P. E. Kauppi et al., Proc. Natl. Acad. Sci. U.S.A. 103, 17574 (2006).
14. Y. Pan et al., Biogeosciences 8, 715 (2011).
15. Y. Pan, R. Birdsey, J. Hom, K. McCullough, For. Ecol. Manage. 259, 151 (2009).
16. P. J. van Mantgem et al., Science 323, 521 (2009).
17. D. D. Breshears et al., Proc. Natl. Acad. Sci. U.S.A. 102, 15144 (2005).
18. P. Ciais et al., Nat. Geosci. 1, 425 (2008).
19. J. Fang, A. Chen, C. Peng, S. Zhao, L. Ci, Science 292, 2320 (2001).
20. S. L. Lewis et al., Nature 457, 1003 (2009).
21. O. L. Phillips et al., Science 323, 1344 (2009).
22. M. Gloor et al., Glob. Change Biol. 15, 2418 (2009).
23. S. L. Lewis, J. Lloyd, S. Sitch, E. T. A. Mitchard, W. F. Laurance, Annu. Rev. Ecol. Syst. 40, 529 (2009).
24. R. A. Houghton, Annu. Rev. Earth Planet. Sci. 35, 313 (2007).
25. P. Friedlingstein et al., Nat. Geosci. 3, 811 (2010).
26. C. Tarnocai et al., Global Biogeochem. Cycles 23, GB2023 (2009).
27. A. Hooijer et al., Biogeosciences 7, 1505 (2010).
28. S. E. Page, J. O. Rieley, C. J. Banks, Glob. Change Biol. 17, 798 (2011).
29. Intergovernmental Panel on Climate Change, IPCC Guidelines for National Greenhouse Gas Inventories (Institute for Global Environmental Strategies, Japan, 2006); www.ipcc-nggip.iges.or.jp/public/2006gl/index.html.
30. A. D. McGuire et al., Ecol. Monogr. 79, 523 (2009).
31. C. L. Goodale et al., Ecol. Appl. 12, 891 (2002).
32. J. L. Sarmiento et al., Biogeosciences 7, 2351 (2010).
33. E. D. Schulze et al., Nat. Geosci. 2, 842 (2009).
34. S. W. Pacala et al., Science 292, 2316 (2001).
35. O. L. Phillips et al., Philos. Trans. R. Soc. London Ser. B 359, 381 (2004).
36. J. M. Metsaranta, W. A. Kurz, E. T. Neilson, G. Stinson, Tellus 62B, 719 (2010).
37. M. Zhao, S. W. Running, Science 329, 940 (2010).
38. R. A. Houghton, Tellus 55B, 378 (2003).

REPORTS

Detection of Emerging Sunspot Regions in the Solar Interior

Stathis Ilonidis,* Junwei Zhao, Alexander Kosovichev

Sunspots are regions where strong magnetic fields emerge from the solar interior and where major eruptive events occur. These energetic events can cause power outages, interrupt telecommunication and navigation services, and pose hazards to astronauts. We detected subsurface signatures of emerging sunspot regions before they appeared on the solar disc. Strong acoustic travel-time anomalies of an order of 12 to 16 seconds were detected as deep as 65,000 kilometers. These anomalies were associated with magnetic structures that emerged with an average speed of 0.3 to 0.6 kilometer per second and caused high peaks in the photospheric magnetic flux rate 1 to 2 days after the detection of the anomalies. Thus, synoptic imaging of subsurface magnetic activity may allow anticipation of large sunspot regions before they become visible, improving space weather forecast.

Understanding solar magnetism is among the most important problems of solar physics and astrophysics (1–5). Modern theories assume that sunspot regions are generated by a dynamo action at the bottom of the convection zone, about 200 Mm below the photosphere. However, there is no convincing observational evidence to support this idea, and dynamo mechanisms operating in the bulk of the convection zone or even in the near-surface shear layer have been proposed as well (6, 7). Investigation of emerging magnetic flux could possibly determine the depth of this process and set the foundations for a better understanding of sunspots and active regions.

Active regions on the Sun produce flares and mass eruptions that may cause power outages on Earth, satellite failures, and interruptions of telecommunication and navigation services. Monitoring solar subsurface processes and predicting magnetic activity would also improve space weather forecasts.

W. W. Hansen Experimental Physics Laboratory, Stanford University, Stanford, CA 94305–4085, USA

*To whom correspondence should be addressed. E-mail: ilonidis@sun.stanford.edu

Time-distance helioseismology (8) is one of the local helioseismology techniques that image acoustic perturbations in the interior of the Sun (9). Acoustic waves are excited by turbulent convection near the surface, propagate deep inside the Sun, and are refracted back to the surface (Fig. 1). Time-distance helioseismology measures travel times of acoustic waves propagating to different distances by computing cross-covariances between the oscillation signals observed at pairs of locations on the solar photosphere. Variations in acoustic travel times are caused mainly by thermal perturbations, magnetic fields, and flows. Previous studies of emerging sunspot regions (10–14) have found difficulties in detecting signals deeper than 30 Mm and before the initial magnetic field becomes visible on the surface because of the fast emergence speed and low signal-to-noise ratio (15). Here, we present a deep-focus time-distance measurement scheme, which allows us to detect signals of emerging magnetic regions in the deep solar interior (16, 17).

We have used Doppler observations (18) from Michelson Doppler Imager (MDI) (19) onboard the Solar and Heliospheric Observatory (SOHO) and computed travel-time maps of four emerging flux regions and nine quiet regions. In Fig. 2, we present the results of our analysis for Active Region (AR) 10488, which started emerging on the solar disc at 09:30 UT, 26 October 2003, about

30° east of the central meridian. Soon after the start of emergence, the magnetic flux rate steeply increased and had a strong peak on 27 October at about 08:00 UT. A travel-time map, computed from an 8-hour data set and centered at 03:30 UT, 26 October, about 28.5 hours before the peak in flux rate, shows a strong negative travel-time perturbation at the same solar coordinates but deep inside the convection zone. This feature, with maximum travel-time anomaly of 16.3 s (relative to the quiet Sun), was initially observed in the travel-time maps centered at 23:30 UT, 25 October, 10 hours before the start of the active region emergence. During the next 4 to 5 hours

(20), the perturbation increased in size and strength and then gradually weakened over the next 3 to 4 hours (Fig. 2D). No other strong perturbations were detected at the same location before or after the appearance of this perturbation.

ARs 8164 and 8171 emerged in the northern and southern hemispheres at 04:00 UT, 23 February 1998 and 09:30 UT, 27 February 1998, respectively. They were both smaller and less active than AR 10488. The total unsigned magnetic flux and the flux rate of AR 8164 reveal that most of the flux emerged during a period of 2 days, with a strong peak in the flux rate around 08:00 UT, 24 February (Fig. 3D). The

travel-time map of Fig. 3A, computed from an 8-hour data set centered at 00:00 UT, 23 February, shows a strong signature of the emerging flux, with the maximum travel-time anomaly of 14.0 s. A similar signature, with the peak value of 12.5 s, appeared in the travel-time map of AR 8171 for a data set centered at 04:30 UT, 27 February (fig. S2). These signatures first appeared several hours before the start of magnetic field emergence in the photosphere and at least 30 hours before the corresponding peaks in the flux rate.

Active Region 7978 emerged in the southern hemisphere at 17:00 UT, 06 July 1996. It continued to grow for the next 3 days, even though the magnetic flux rate (Fig. 4D) was not as steep as in the previous cases. The travel-time map of Fig. 4A, centered at 11:30 UT, 06 July, displays a strong perturbation at the location of the emergence with a maximum travel-time anomaly of 11.9 s.

All of our measurements were carried out either in quiet-Sun regions, before the start of emergence, or in emerging flux regions where magnetic fields higher than 300 G had been masked. The travel-time anomalies of Figs. 2 to 4 were all detected before the start of emergence, and therefore they could not have been caused by surface magnetism effects (21, 22). The sample of four emerging flux events includes sunspot regions of different size and total magnetic flux, which were observed at different locations on the solar disc during different phases of the solar cycle. In all of these cases, the perturbation index shows high peaks only for a narrow time interval of the pre-emergence phase, but it stays very low after the start of emergence (Figs. 2D, 3D, and 4D and fig. S2D). This indicates that strong emerging flux events are detectable by our method. Indeed, our results show that 1 to 2 days after the detected anomalies, the magnetic structures associated with these anomalies reach the surface and cause high peaks in the photospheric magnetic flux rates. An emerging time of ~2 days from a depth of ~60 Mm is also consistent with numerical simulation models of emerging flux [figure 18 of (2)]. Our results also show an anticorrelation between the height of the perturbation index peak and the time lag between this peak and the peak in the flux rate. Thus, higher peaks in the perturbation index may be caused by stronger magnetic fields that are more buoyant and rise to the surface faster.

In order to test the statistical significance of our results, we used the same method to analyze nine data sets of quiet-Sun regions, with no emerging flux events. The sample of nine regions was selected from three different phases of the solar cycle and covers several locations of the solar disc up to 45° away from the disc center. These regions did not show substantial travel-time anomalies. The measured travel-time perturbations follow a Gaussian distribution with a SD of ~3.3 s (fig. S3), which is 3.6 to 4.9 times smaller than the peak signal of emerging flux regions. Such perturbations can be caused by realization noise, thermal variations, and weaker magnetic field structures that did not emerge soon in the photosphere.
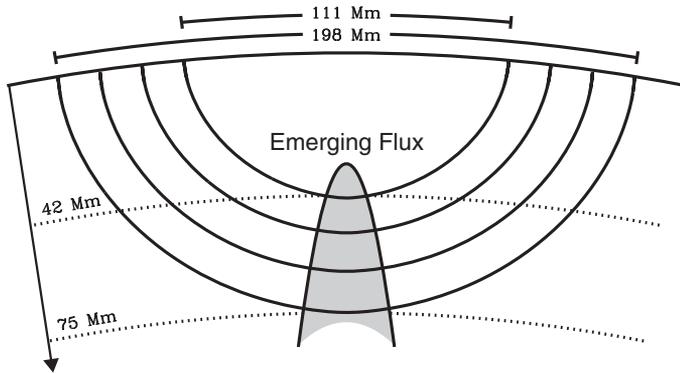

Fig. 1. Acoustic ray paths with lower turning points between 42 and 75 Mm crossing a region of emerging flux. For simplicity, only four out of a total of 31 ray paths used in this study are shown here.
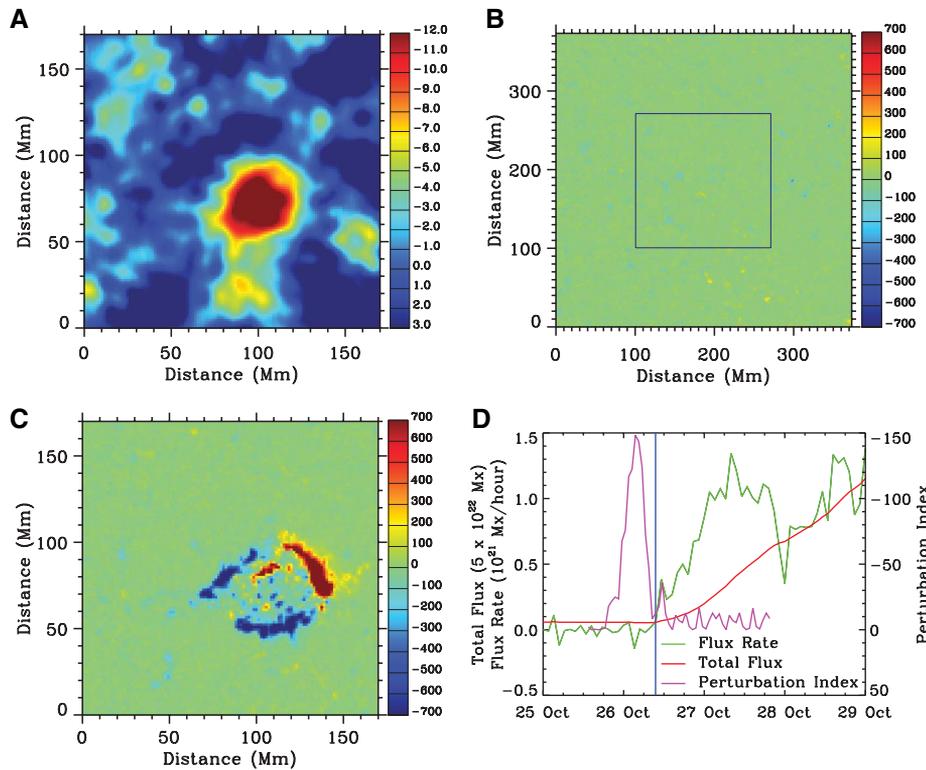

Fig. 2. (A) Mean travel-time perturbation map (in seconds) of AR 10488 at a depth of 42 to 75 Mm, obtained from an 8-hour data set centered at 03:30 UT, 26 October 2003. (B) Photospheric magnetic field (in gauss) at the same time as (A). The whole map corresponds to the region where the computations were carried out, whereas the squared area at the center corresponds to the region shown in (A). (C) Photospheric magnetic field (in gauss) at the same location as (A) but 24 hours later. (D) Total unsigned magnetic flux (red line) and magnetic flux rate (green line) of AR 10488. The vertical blue line marks the start of emergence. The pink line shows the temporal evolution of the perturbation index (in units of 125 s Mm²), which is defined as the sum of travel-time perturbations with values lower than −5.4 s, within the signature of (A).

The detection of sunspot regions deep inside the convection zone, by means of local helioseismology, has scientific as well as practical implications. Maps of the travel-time anomalies show that the signatures of emerging flux are mostly concentrated in circular areas with a typ-

ical size of 30 to 50 Mm. The horizontal wavelength of the acoustic waves at this depth is about 35 Mm, which poses limits on the size of subsurface structures that can be resolved as well as on the accuracy of the location of detected perturbations. This may also explain the

absence of two distinct signatures—associated with the two magnetic polarities of sunspot regions—in the travel-time maps. At the start of emergence in the photosphere, the two polarities are observed very close to each other, and only after this stage they progressively form

Fig. 3. (**A**) Mean travel-time perturbation map (in seconds) of AR 8164 at a depth of 42 to 75 Mm, obtained from an 8-hour data set centered at 00:00 UT, 23 February 1998. (**B**) Photospheric magnetic field (in gauss) at the same time as (A). The whole map corresponds to the region where the computations were carried out, whereas the squared area at the center corresponds to the region shown in (A). (**C**) Photospheric magnetic field (in gauss) at the same location as (A) but 24 hours later. (**D**) Total unsigned magnetic flux (red line) and magnetic flux rate (green line) of AR 8164. The lines and units are as in Fig. 2.
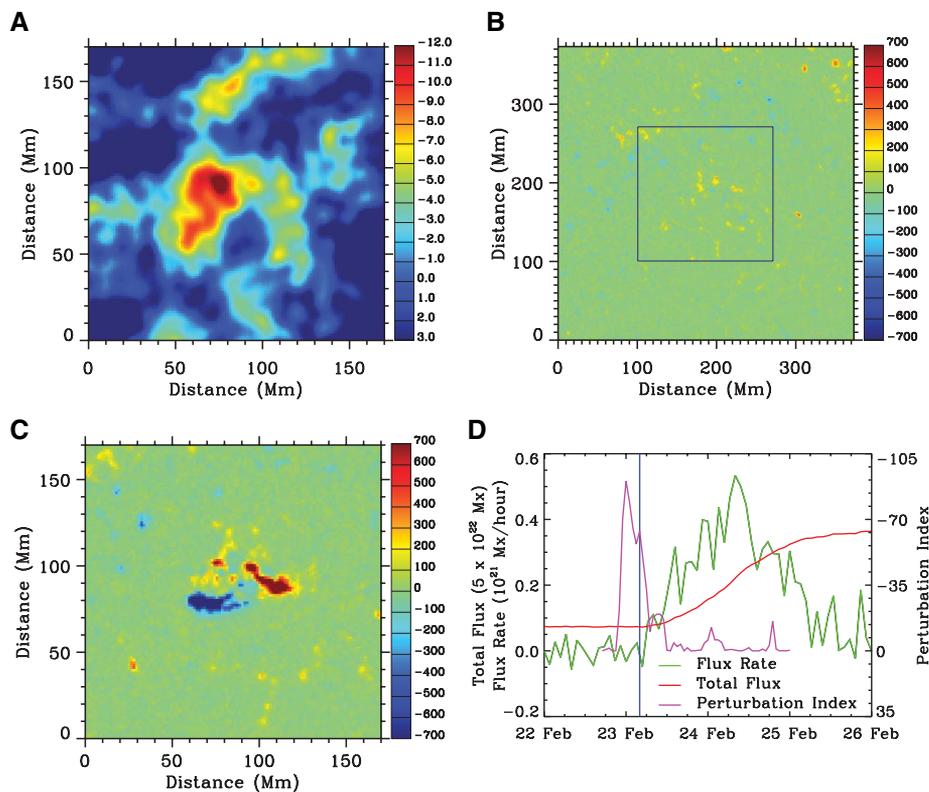

Fig. 4. (**A**) Mean travel-time perturbation map (in seconds) of AR 7978 at a depth of 42 to 75 Mm, obtained from an 8-hour data set centered at 11:30 UT, 06 July 1996. (**B**) Photospheric magnetic field (in gauss) at the same time as (A). The whole map corresponds to the region where the computations were carried out, whereas the squared area at the center corresponds to the region shown in (A). (**C**) Photospheric magnetic field (in gauss) at the same location as (A) but 24 hours later. (**D**) Total unsigned magnetic flux (red line) and magnetic flux rate (green line) of AR 7978. The lines and units are as in Fig. 2.
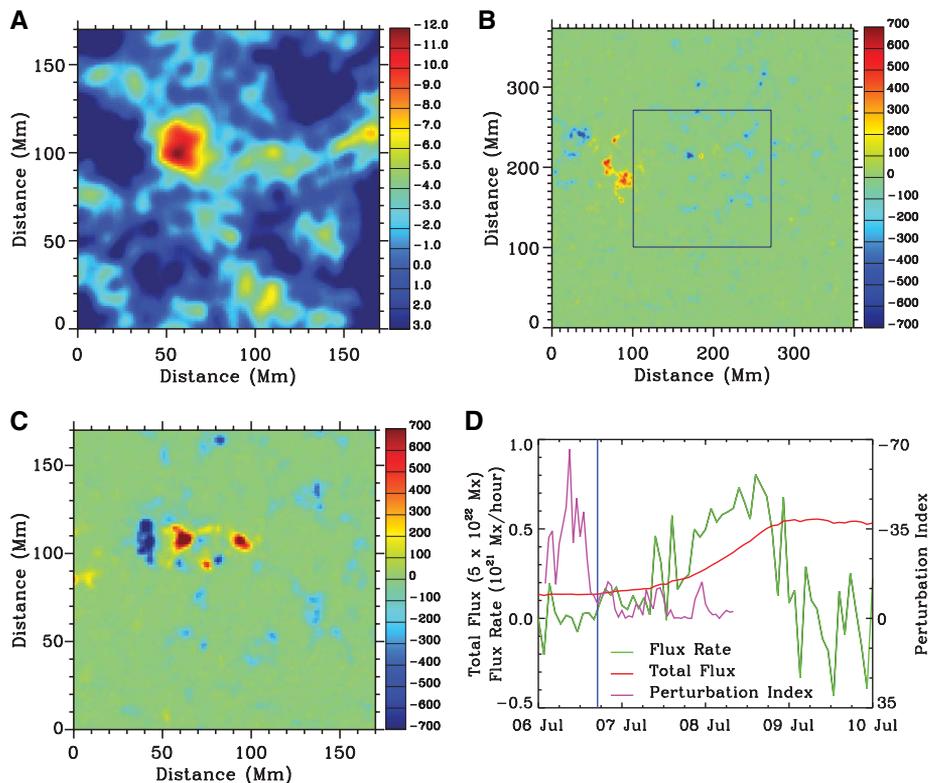
an elongated bipolar feature. The travel-time perturbations caused by the four events are all negative, with the maximum amplitude of 16.3 s. This is surprisingly strong. Recent theoretical studies, based on numerical simulations of emerging magnetic flux tubes, estimate the magnitude of travel-time anomalies at these depths to be of an order of 1 s (23). This discrepancy may imply that the magnetic field deep inside the convection zone is much stronger than in the models or that the magnetic field effects in the acoustic travel times are not yet well understood. However, the nature of the perturbations are not known, and the detected anomalies can be due to thermal rather than magnetic effects. In addition, a weak magnetic flux at large depths is probably unde-tectable by our method. Therefore, the disappear-ance of the travel-time anomalies after the start of emergence does not necessarily imply that sun-spots are disconnected from their roots.

Our measurements and tests with several phase-speed filters also show that acoustic waves focused at depths of about 57 to 66 Mm have the biggest contribution to the signatures of emerging flux. The detection of such signatures at a depth of about 60 Mm possibly poses a low limit on the depth of generation of large magnetic regions. The average emergence speed from this depth up to the surface is estimated to be ~0.3 and 0.6 km/s for the analyzed weakest and strongest emerging flux events, respectively.

Predicting solar magnetic activity is a valu-able tool for space weather forecasts. Our tech-nique of imaging the deep solar interior, combined with uninterrupted helioseismic observations of the Solar Dynamics Observatory and the far-side imaging technique (24–26), can monitor the Sun's activity in a synoptic way, both in the near and the far sides, and allow detection of large sunspot regions before their appearance on the solar disc. Strong emerging flux events can now be anticipated 1 to 2 days in advance.

below the center of the annulus. Thus, the inferred travel-time variations essentially map local inhomogeneities around the focal point. By moving the center of the annulus to neighboring points of the observed area, it is possible to make a map of travel-time perturbations at a fixed depth.

16. In our approach, the oscillation signal is first averaged over an arc, and then cross-covariances are computed for every pair of diametrically opposite averaged arcs. This procedure has been already used, with an arc size of 90°, to determine the coefficients of absorption, emissivity reduction, and local suppression inside sunspots (28). In this configuration, every point in the annulus contributes to the oscillation signal of one and only one arc (fig. S1). Here, we select arcs of five different sizes—25.7°, 30°, 36°, 45°, and 60°—and average the corresponding cross-covariances in order to reduce the noise level. The position of the arcs along the annulus can be chosen arbitrarily. However, in order to eliminate anisotropic contributions in the computation of cross-covariances and further increase the signal-to-noise ratio, four different arc orientations are chosen for each of the five arc sizes. The orientations are determined so that starting from an arbitrary point, each one can be produced from the previous one by a fixed rotation, which depends on the arc size. If the arc size is N degrees, the rotation angle is $N/4$ degrees. In total, there are 20 configurations; each one is characterized by one of the five arc sizes and one of the four orientations for the given arc size.

17. We computed cross-covariances for every pair of diametrically opposite arcs using all of the 20 configurations described in (16) and repeated this procedure for 31 annuli, spanning a radius range of 55.5 to 99.0 Mm (Fig. 1). We then added all of the cross-covariances together and fitted the final cross-covariance with a Gabor wavelet (29) so as to determine the acoustic-phase travel time at a single pixel. If the same procedure is repeated for all pixels in the observed area, an acoustic travel-time map can be constructed. The signal-to-noise ratio of the travel-time map depends on the number of ray paths focused below the photosphere, and our results show that averaging over the 20 configurations and the 31 travel distances is sufficient to detect large emerging magnetic structures. It should also be noted that cross-covariances obtained from different travel distances have different phases and therefore can be added together only after appropriate travel-time shifts. We determined these travel-time shifts from the quiet-Sun measurements and made sure that no phase-shift cancellation occurs.

18. The data sets are 8-hour-long series of dopplergrams, tracked with a Carrington rotation rate and remapped into heliographic coordinates by using Postel's projection. The size of the tracked region is 256 by 256 pixels, with a spatial resolution of 0.12°/pixel. Each data set is filtered in the Fourier domain in order to extract the solar acoustic oscillation signals in the frequency range of 2 to 5 mHz, with phase speeds of 92 to 127 km/s. These waves have a 1-skip horizontal distance of 111 to 198 Mm, sampling the Sun's interior up to depths of 42 to 75 Mm (Fig. 1).
19. P. H. Scherrer et al., Sol. Phys. **162**, 129 (1995).
20. We always refer to middle time of an 8-hour data set unless otherwise stated.
21. C. Lindsey, D. C. Braun, Astrophys. J. **620**, 1107 (2005).
22. J. Zhao, A. G. Kosovichev, Astrophys. J. **643**, 1317 (2006).
23. A. C. Birch, D. C. Braun, Y. Fan, Astrophys. J. **723**, L190 (2010).
24. C. Lindsey, D. C. Braun, Science **287**, 1799 (2000).
25. J. Zhao, Astrophys. J. **664**, L139 (2007).
26. S. Ilonidis, J. Zhao, T. Hartlep, Sol. Phys. **258**, 181 (2009).
27. T. L. Duvall Jr., in Proc. GONG '94: Helio- and Astero-Seismology from the Earth and Space, R. K. Ulrich, E. J. Rhodes Jr., W. Dappen, Eds. (ASPCS, San Francisco 1995), p. 76.
28. S. Ilonidis, J. Zhao, Sol. Phys. **268**, 377 (2011).
29. A. G. Kosovichev, T. L. Duvall, Jr., in Proc. SCORe96 Workshop: Solar Convection and Oscillations and Their Relationship, F.P. Pijpers, J. Christensen-Dalsgaard, C.S. Rosenthal, Eds. (Kluwer, Dordrecht, 1996), 241.

Quantum Simulation of Frustrated Classical Magnetism in Triangular Optical Lattices

J. Struck,[1] C. Ölschläger,[1] R. Le Targat,[1] P. Soltan-Panahi,[1] A. Eckardt,[2] M. Lewenstein,[2,3] P. Windpassinger,[1] K. Sengstock[1]*

Magnetism plays a key role in modern technology and stimulates research in several branches of condensed matter physics. Although the theory of classical magnetism is well developed, the demonstration of a widely tunable experimental system has remained an elusive goal. Here, we present the realization of a large-scale simulator for classical magnetism on a triangular lattice by exploiting the particular properties of a quantum system. We use the motional degrees of freedom of atoms trapped in an optical lattice to simulate a large variety of magnetic phases: ferromagnetic, antiferromagnetic, and even frustrated spin configurations. A rich phase diagram is revealed with different types of phase transitions. Our results provide a route to study highly debated phases like spin-liquids as well as the dynamics of quantum phase transitions.

Frustrated spin systems belong to the most demanding problems of magnetism and condensed matter physics (1, 2). The sim-plest realization of geometrical spin frustration is the triangular lattice (Fig. 1) with antiferromag-netic interactions: The spins cannot order in the favored antiparallel fashion and instead must compromise. The rich variety of possible spin